

Field-controllable giant spin relaxation anisotropy in (hBN)/graphene/hBN heterostructures

Klaus Zollner,^{1,*} Martin Gmitra,² and Jaroslav Fabian¹

¹*Institute for Theoretical Physics, University of Regensburg, 93040 Regensburg, Germany*

²*Institute of Physics, P. J. Šafárik University in Košice, 04001 Košice, Slovakia*

(Dated: July 8, 2024)

It is predicted that heterostructures of monolayer graphene and hexagonal boron nitride (hBN) exhibit a giant and electrically tunable spin relaxation (SR) anisotropy (ratio of out-of-plane to in-plane spin lifetimes). Combining extensive first-principles calculations for (hBN)/graphene/hBN stacks with a minimal tight-binding model, we extract orbital and spin-orbit coupling (SOC) parameters of the proximitized graphene. Our calculations show that the parameters depend strongly on a transverse electric field, but also on stacking configurations and interlayer distances, giving a rich playground for spin physics. The SR anisotropy is found to be giant close to the charge neutrality point, decreasing with increasing doping, and being highly field tunable.

PACS numbers: 72.80.Vp, 73.22.Pr, 71.70.Ej, 85.75.-d

Keywords: spintronics, graphene, heterostructures, proximity spin-orbit coupling

Introduction. Graphene encapsulated in hBN is emerging as the long-awaited platform for two-dimensional (2D) spintronics [1, 2]. The first generation of graphene devices — based on graphene on substrates such as SiO₂ — show ultrafast spin relaxation [3–7] with spin lifetimes on the order of 0.1–1 ns. The absence of a marked spin relaxation anisotropy in these devices [8–10] was explained by the presence of magnetic resonant scatterers [11]. The new generation of graphene devices is based on (hBN)/graphene/hBN stacks [12–24], which have mobilities up to 10⁶ cm²/Vs [25–27] and record spin lifetimes exceeding 10 ns [17].

There is now experimental evidence that in hBN encapsulated *bilayer graphene*, SR is due to SOC [28, 29]. Finally there is a graphene-based structure in which spins live long (10 ns) and SOC is strong enough (relative to other spin-dependent interactions) to play a dominant role and be used for spin manipulation. The evidence comes from SR anisotropy. In 2D electron gases in semiconductor quantum wells the out-of-plane electron spins have lifetimes ($\tau_{s,z}$) smaller than in-plane spins ($\tau_{s,x}$), due to the in-plane Rashba fields [2]. Typically the SR anisotropy ratio $\xi = \tau_{s,z}/\tau_{s,x}$ is 0.5, reflecting the fact that two spin-orbit field components can flip an out-of-plane spin, but only one component can flip the in-plane spin. In contrast, as recently predicted [30] and soon experimentally realized [28, 29, 31, 32], 2D materials offer so far unrivaled control over ξ . It was found that graphene on a transition metal dichalcogenide (TMDC) has $\xi \approx 10$, due to the strong valley Zeeman spin-orbit fields, being induced from the TMDC into graphene. In this system the spin-orbit fields are relatively large (1 meV [33]) compared to graphene (10 μ eV [34]), which is also reflected in the rather small spin lifetimes of about 10 ps.

On the other hand, the SR anisotropy in encapsulated bilayer graphene is also giant ($\xi \approx 10$), but the spin life-

time is three orders of magnitude larger, up to 10 ns [28, 29]. Remarkably, the SR anisotropy ξ sharply *increases* as a transverse electric field is applied [29] at a fixed doping. This is counter-intuitive, since the applied field should increase the Rashba field and lower $\tau_{s,z}$. The resolution lies in the idiosyncratic spin-orbit band structure of bilayer graphene. In the presence of even a moderate electric field, the lowest energy bands at K split due to SOC, but the splitting does not depend on the field, acquiring the intrinsic value of about 24 μ eV [35], determined by density-functional theory (DFT).

Here we focus on monolayer graphene encapsulated in hBN, or placed on a hBN substrate. We predict, by DFT calculations and phenomenological modeling, the values of induced spin-orbit fields, as well as what is the expected SR anisotropy in a variety of potentially realizable structures. It is shown (and this should be true for bilayer graphene at low electric fields as well) that the anisotropy depends on the actual atomic arrangement of the structures, and is highly electrically tunable. Unlike in bilayer graphene, in our systems the anisotropy ξ *decreases* with increasing electric field, being giant (about 10) at low fields and reaching the Rashba limit of 50% at large fields. The spin lifetimes are expected to be on the order of 10 ns, as already seen experimentally, and also theoretically elaborated for SOC in the tens of μ eV range [36].

Electronic band structure. The lattice constants of graphene and hBN differ by less than 2%, justifying theoretical considerations of commensurate geometries. While the small lattice mismatch does lead to moiré patterns [37–39], the global band structure of the stacks is qualitatively similar [40, 41]. Nevertheless, here we consider all structural arrangements for commensurate unit cells so as to get quantitative feeling for spin-orbit phenomena in a generic experimental setting. Below we discuss in detail one representative structure (C1, see below)

for hBN encapsulated graphene, while presenting data of all structures (also graphene on hBN) in a tabular form.

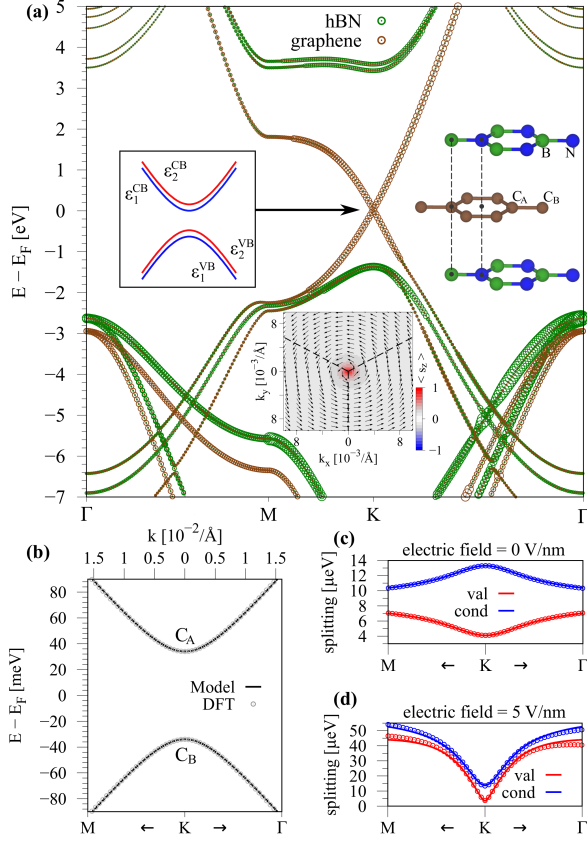


FIG. 1. (Color online) (a) Calculated electronic band structure of hBN encapsulated graphene. The bands of graphene (hBN) are plotted in brown (green). The right inset shows the geometry for $(H\alpha H, B\beta B) = C1$ configuration, being the energetically favorable one of hBN encapsulated graphene. The left inset shows a sketch of the low energy dispersion close to the K point. Due to the presence of the substrate, graphene's low energy bands are split into four states $\varepsilon_{1/2}^{CB/VB}$, with a band gap. (b) Calculated low energy dispersion close to the K point (symbols) with a fit to our model Hamiltonian (solid line). The conduction (valence) band is formed by C_A (C_B) sublattice. (c) Spin-orbit splittings of the conduction (blue) and valence (red) band for transverse electric field of 0 V/nm. (d) Same as (c), but for finite electric field of 5 V/nm. The lower inset in (a) shows the corresponding spin-orbit field for ε_2^{VB} and an applied electric field of 5 V/nm.

First, we define a terminology to make sense of the structural arrangements. We denote the three relevant sites in hBN as the B-site (Boron), the N-site (Nitrogen), and the H-site (hollow position in the center of the hexagon). Similarly, we have two graphene sublattices α (C_A) and β (C_B). A stacking sequence is then abbreviated as $(U\alpha V, X\beta Y)$, indicating that the α (β) sublattice of graphene is sandwiched between the U and V (X and Y) sites of top and bottom hBN, each of which can take the values $\{B, N, H\}$. It has been shown [40],

that the energetically most favorable sandwich structure is $(H\alpha H, B\beta B)$ in agreement with our findings, see Tab. I, meaning that α (β) is sandwiched between the two H-sites (B-sites) of top and bottom hBN. From now on, we refer to the lowest-energy stacking geometry $(H\alpha H, B\beta B)$ as the C1 configuration, whose structure is shown in the right inset of Fig. 1(a). Interlayer distances were obtained by a distance study [42].

The calculated band structure of encapsulated graphene in the C1 configuration is shown in Fig. 1(a). Other stacking geometries exhibit similar band features. The Dirac bands of graphene are located within the hBN band gap. Since the structure has broken pseudospin symmetry, a band gap of about 70 meV opens in graphene; C_A orbitals form the conduction band (CB), while C_B ones form the valence band (VB). Further, the low energy bands split into four states $\varepsilon_{1/2}^{CB/VB}$ due to SOC and the Rashba effect, see left inset in Fig. 1(a) and Fig. 1(b), where we show the low energy band structure with a fit to our model Hamiltonian (see below). We denote the spin-orbit splittings of the bands, which are in the μeV range, as $\Delta E_{CB} = \varepsilon_2^{CB} - \varepsilon_1^{CB}$ for CB and $\Delta E_{VB} = \varepsilon_2^{VB} - \varepsilon_1^{VB}$ for VB, and extract them in Fig. 1(c).

Important, the spin-orbit effects can be controlled electrically. In Fig. 1(d) we show the spin-orbit splittings of the bands, in the presence of an external transverse electric field of 5 V/nm, applied across the heterostructure. The spin-orbit field, corresponding to the band ε_2^{VB} , shows a very pronounced Rashba SOC pattern with a peaked s_z -expectation value K , see lower inset in Fig. 1(a). Not only the magnitudes of the splittings change significantly upon applying electric field, also the k -dependence is reversed for the CB, indicating unusually large tunability, considering that we deal with monolayer graphene.

Model Hamiltonian. The band structure of proximitized graphene can be modeled by symmetry-derived Hamiltonians [43]. In particular, for (hBN)/graphene/hBN heterostructures having C_{3v} symmetry, the effective low energy band Hamiltonian is

$$\mathcal{H} = \mathcal{H}_0 + \mathcal{H}_\Delta + \mathcal{H}_I + \mathcal{H}_R + \mathcal{H}_{PIA}, \quad (1)$$

$$\mathcal{H}_0 = \hbar v_F (\tau k_x \sigma_x - k_y \sigma_y) \otimes s_0, \quad (2)$$

$$\mathcal{H}_\Delta = \Delta \sigma_z \otimes s_0, \quad (3)$$

$$\mathcal{H}_I = \tau (\lambda_I^A \sigma_+ + \lambda_I^B \sigma_-) \otimes s_z, \quad (4)$$

$$\mathcal{H}_R = -\lambda_R (\tau \sigma_x \otimes s_y + \sigma_y \otimes s_x), \quad (5)$$

$$\mathcal{H}_{PIA} = a (\lambda_{PIA}^A \sigma_+ - \lambda_{PIA}^B \sigma_-) \otimes (k_x s_y - k_y s_x). \quad (6)$$

Here v_F is the Fermi velocity and the in-plane wave vector components k_x and k_y are measured from $\pm K$, corresponding to the valley index $\tau = \pm 1$. The Pauli spin matrices are s_i , acting on spin space (\uparrow, \downarrow), and σ_i are pseudospin matrices, acting on sublattice space (C_A, C_B), with $i = \{0, x, y, z\}$ and $\sigma_\pm = \frac{1}{2}(\sigma_z \pm \sigma_0)$. The lattice constant is $a = 2.46 \text{ \AA}$ of pristine graphene and the stag-

gered potential gap is Δ . The parameters λ_I^A and λ_I^B describe the sublattice resolved intrinsic SOC, λ_R stands for the Rashba SOC, and λ_{PIA}^A and λ_{PIA}^B are for the sublattice resolved pseudospin-inversion asymmetry (PIA) SOC. The basis states are $|\Psi_{A,\uparrow}\rangle$, $|\Psi_{A,\downarrow}\rangle$, $|\Psi_{B,\uparrow}\rangle$, and $|\Psi_{B,\downarrow}\rangle$, resulting in four eigenvalues $\varepsilon_{1/2}^{CB/VB}$.

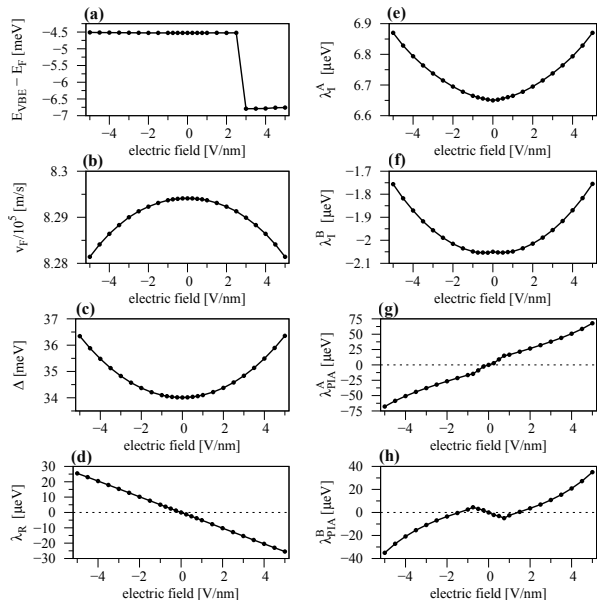


FIG. 2. (Color online) Fit parameters as a function of the applied transverse electric field for the C1-configuration. (a) Valence band edge with respect to the Fermi level, (b) Fermi velocity v_F , (c) gap parameter Δ , (d) Rashba SOC parameter λ_R , (e,f) intrinsic SOC parameters λ_I^A and λ_I^B , and (g,h) PIA SOC parameters λ_{PIA}^A and λ_{PIA}^B .

The C1 configuration at zero electric field has mirror symmetry, reflected in the D_{3h} symmetric version of the Hamiltonian with vanishing Rashba and PIA contributions 43. Parameters, best fitting the DFT results (Fig. 1 shows that the model perfectly fits), are given in Tab. I, where we also include other possible configurations of hBN encapsulated graphene, also including hBN/graphene/2hBN examples. Overall, the magnitudes of SOCs are tens of μeV , while the parameters can differ (also in sign) from structure to structure. For example, the (H α B, B β H) configuration is in the D_{3d} subgroup and the only allowed SOC parameters are $\lambda_I^A = \lambda_I^B$. In this case the orbital gap $\Delta = 0$, since the overall potential, from top and bottom hBN layer, is equal for the two graphene sublattices.

Tunability of the parameters for C1, by electric field, is shown in Fig. 2. The Rashba and PIA parameters — which are due to inversion asymmetry — are odd functions (almost linear) of electric field and strongly tunable. In contrast, the orbital parameters v_F and Δ , as well as intrinsic SOC parameters λ_I^A and λ_I^B are even functions and only weakly affected by the field. Applying an external field, we find a linear tunability of roughly 5 μeV

per V/nm of λ_R , similar to freestanding graphene [34], which is expected for the mirror-symmetric C1.

Similarly, we calculated different stacking configurations for graphene on hBN. The extracted band-structure parameters are in Tab. II for three commensurate high-symmetry graphene/hBN stacking configurations, with their corresponding lowest energy distance [42]. The energetically most favorable stacking configuration is (α B, β H), which shows a similar tunability of λ_R by applying an external field [42]. The Rashba coupling is stronger than for encapsulated graphene, reflecting enhanced inversion asymmetry.

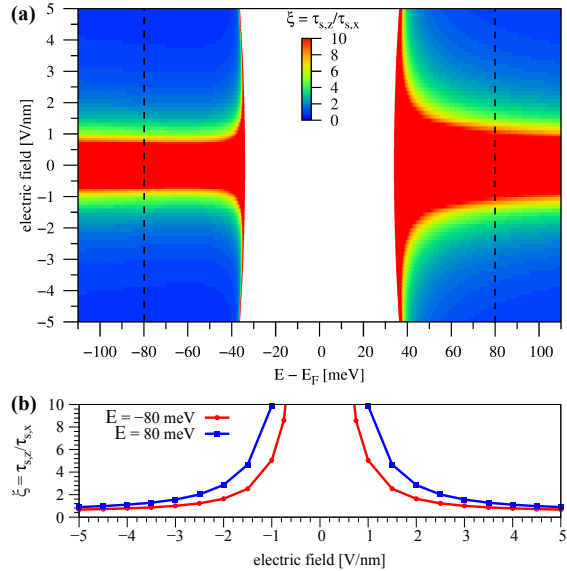


FIG. 3. (Color online) (a) Calculated SR anisotropy $\xi = \tau_{s,z}/\tau_{s,x}$ as function of energy and applied transverse electric field for C1-configuration of hBN encapsulated graphene, using $\tau_p = 125$ fs and $\tau_{iv} = 8 \cdot \tau_p$. (b) Anisotropy ξ at energies $E = \pm 80$ meV corresponding to the dashed lines in (a).

Spin Relaxation Anisotropy. While experimental spectral sensitivities approach the limits of tens of μeV for encapsulated graphene, making the above calculations relevant for sensitive mesoscopic transport measurements, the most striking ramifications of the obtained spin-orbit tunability is expected to be in SR anisotropy, which has been a hotly debated issue recently. Indeed, we predict a wide electrical tunability of the SR time of this basic structure. Since the low energy Hamiltonian \mathcal{H} can nicely reproduce the dispersion, splittings and spin expectation values [42], see Fig. 1(b-d), we can use it together with our parameters to calculate SR times. To get representative quantitative estimates, we take the momentum relaxation time $\tau_p = 125$ fs and a variable intervalley scattering time τ_{iv} . It is straightforward to obtain the anisotropies for actual experimental values of the scattering times, using our tabulated results. The SR anisotropy is then $\xi = \tau_{s,z}/\tau_{s,x}$, with the SR times for the out-of-plane, $\tau_{s,z}$, and in-plane spins, $\tau_{s,x}$, evalu-

Configuration	ΔE [meV]	$v_F/10^5$ [$\frac{m}{s}$]	Δ [meV]	λ_R [μeV]	λ_I^A [μeV]	λ_I^B [μeV]	λ_{PIA}^A [μeV]	λ_{PIA}^B [μeV]
(H α B, B β H)	0.01	8.296	0	0	2.19	2.19	0	0
(H α N, N β H)	26.60	8.068	0	0	13.31	13.31	0	0
(N α B, B β N)	32.05	7.931	0	0	15.76	15.76	0	0
(H α H, B β B) = C1	0	8.294	34.24	0	6.65	-2.05	0	0
(N α N, H β H)	26.09	8.070	34.10	0	11.38	15.47	0	0
(B α B, N β N)	31.76	7.932	-48.00	0	18.95	12.34	0	0
(H α B, N β H)	13.12	8.175	-34.85	-1.97	6.51	9.05	3.15	31.35
(N α B, B β H)	15.89	8.110	6.29	-7.75	5.09	12.84	1.26	22.72
(B α N, N β H)	29.20	7.998	-6.50	-4.97	15.23	13.92	-61.34	49.22
(N α B, H β H)	13.16	8.176	-0.069	-2.58	4.76	11.01	16.02	15.98
(B α B, N β H)	15.85	8.108	-41.50	-7.37	8.31	9.55	6.71	16.36
(N α N, B β H)	28.82	8.000	41.14	-3.29	11.89	17.26	94.83	-106.79
(H α BN, B β HH)	0.07	8.296	0.093	0.40	2.06	2.22	0	0
(B α BN, H β HH)	0	8.298	-34.06	0.31	-2.23	6.66	0	0

TABLE I. Fit parameters of Hamiltonian \mathcal{H} , for different stacking configurations of hBN encapsulated graphene, using the energetically most favorable graphene-hBN interlayer distances. The energy difference ΔE with respect to the (H α H, B β B) configuration, the Fermi velocity v_F , gap parameter Δ , Rashba SOC parameter λ_R , intrinsic SOC parameters λ_I^A and λ_I^B , and PIA SOC parameters λ_{PIA}^A and λ_{PIA}^B . In the case of hBN/graphene/2hBN, the energy difference is with respect to the (B α BN, H β HH) configuration.

Configuration	distance [\AA]	$v_F/10^5$ [$\frac{m}{s}$]	Δ [meV]	λ_R [μeV]	λ_I^A [μeV]	λ_I^B [μeV]	λ_{PIA}^A [μeV]	λ_{PIA}^B [μeV]
(α B, β H)	3.35	8.308	-17.08	10.65	5.00	9.37	33.58	37.57
(α N, β H)	3.50	8.197	16.31	12.67	11.78	13.96	4.431	26.68
(α N, β B)	3.55	8.128	23.50	17.89	12.21	15.82	12.91	29.73
average	3.47	8.211	7.577	13.74	9.66	13.05	16.97	31.33

TABLE II. Fit parameters of Hamiltonian \mathcal{H} , for the three stacking configurations of graphene on hBN, and for the energetically most favorable distance obtained from our distance study. The Fermi velocity v_F , gap parameter Δ , Rashba SOC parameter λ_R , intrinsic SOC parameters λ_I^A and λ_I^B , and PIA SOC parameters λ_{PIA}^A and λ_{PIA}^B . In the last row we take the average over the configurations for each parameter.

ated using the Dyakonov-Perel formalism [42].

In Fig. 3 we show the SR anisotropy ξ , specifically for C1, as function of Fermi energy and applied transverse electric field. We find that the anisotropy is strongly tunable by both the field and the doping level. At 0 V/nm the anisotropy is giant due to $\lambda_R = 0$, as shown in Fig. 2(d), so that spin-orbit fields are out of plane. As the applied field increases, the anisotropy decreases. Overall, the anisotropy can be tuned electrically from the usual 2D Rashba limit (0.5), to the opposite case of strong out-of-plane fields ($\xi \gg 1$), for a fixed doping, see Fig. 3(b). This is an unprecedented tunability for an electronic system. Curiously, the SR anisotropy decreases with increasing electric field (for a fixed doping), while in encapsulated bilayers the opposite was found [29]. The reason is that in bilayer graphene the spin-splitting at K is not tunable beyond a certain threshold, at marked contrast to single-layer graphene.

For completeness, we also show the SR anisotropy of C1, in Fig. 4, as a function of $N = \tau_{iv}/\tau_p$ and the energy for fixed electric field of 1 V/nm. The individual SR times are up to 100 ns close to the band edges,

see Fig. 4(b), since the hBN encapsulated graphene has quite weak Rashba SOC, leading to a small splitting of the bands. The anisotropy is strongly pronounced close to the band edges and decreases with increasing the carrier density, i.e. the Fermi level. Depending on the exact intervalley scattering time τ_{iv} and carrier density, an anisotropy change within one order of magnitude can be realized.

Conclusions. We performed DFT calculations on hBN encapsulated graphene and graphene on hBN to extract useful orbital and spin-orbital parameters as functions of a transverse electric field, revealing large tunability. The calculated SR times exhibit giant and tunable anisotropies, which are experimentally testable fingerprints of the ultimate role of SOC in SR in graphene.

This work was supported by DFG SPP 1666, SFB 1277 (A09), the European Unions Horizon 2020 research and innovation program under Grant No. 785219, and by the reintegration scheme MSVVaS SR 90/CVTISR/2018 and VVGS-2018-887.

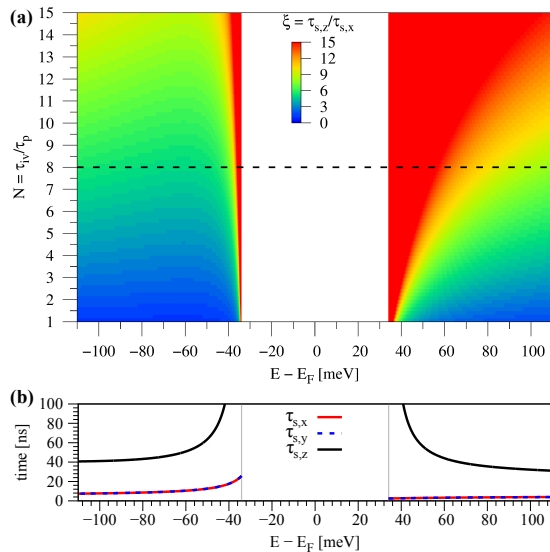


FIG. 4. (Color online) Calculated SR times and anisotropies for CI-configuration and an electric field of 1 V/nm. (a) SR anisotropy $\xi = \tau_{s,z}/\tau_{s,x}$ as a function of $N = \tau_{iv}/\tau_p$ and the energy. (b) Individual SR times as function of energy corresponding to the dashed line in (a) with $\tau_p = 125$ fs and $\tau_{iv} = 8 \cdot \tau_p$. The grey lines indicate the band edges.

* klaus.zollner@physik.uni-regensburg.de

- [1] W. Han, R. K. Kawakami, M. Gmitra, and J. Fabian, *Nat. Nano.* **9**, 794 (2014).
- [2] I. Žutić, J. Fabian, and S. Das Sarma, *Rev. Mod. Phys.* **76**, 323 (2004).
- [3] W. Han, K. Pi, K. M. McCreary, Y. Li, J. J. I. Wong, A. G. Swartz, and R. K. Kawakami, *Phys. Rev. Lett.* **105**, 167202 (2010).
- [4] L. Wang, I. Meric, P. Y. Huang, Q. Gao, Y. Gao, H. Tran, T. Taniguchi, K. Watanabe, L. M. Campos, D. A. Muller, J. Guo, P. Kim, J. Hone, K. L. Shepard, and C. R. Dean, *Science* **342**, 614 (2013).
- [5] T. Maassen, F. K. Dejene, M. H. D. Guimarães, C. Józsa, and B. J. van Wees, *Phys. Rev. B* **83**, 115410 (2011).
- [6] T.-Y. Yang, J. Balakrishnan, F. Volmer, A. Avsar, M. Jaiswal, J. Samm, S. R. Ali, A. Pachoud, M. Zeng, M. Popinciuc, G. Güntherodt, B. Beschoten, and B. Özyilmaz, *Phys. Rev. Lett.* **107**, 047206 (2011).
- [7] N. Tombros, C. Józsa, M. Popinciuc, H. T. Jonkman, and B. J. van Wees, *Nature* **448**, 571 (2007).
- [8] B. Raes, J. E. Scheerder, M. V. Costache, F. Bonell, J. F. Sierra, J. Cuppens, J. Van De Vondel, and S. O. Valenzuela, *Nature Communications* **7**, 1 (2016).
- [9] S. Ringer, S. Hartl, M. Rosenauer, T. Völkl, M. Kadur, F. Hopperdietzel, D. Weiss, and J. Eroms, *Phys. Rev. B* **97**, 205439 (2018).
- [10] T. Zhu and R. K. Kawakami, *Phys. Rev. B* **97**, 144413 (2018).
- [11] D. Kochan, M. Gmitra, and J. Fabian, *Phys. Rev. Lett.* **112**, 116602 (2014).
- [12] S. Roche, J. Åkerman, B. Beschoten, J.-C. Charlier, M. Chshiev, S. Prasad Dash, B. Dlubak, J. Fabian, A. Fert, M. Guimarães, F. Guinea, I. Grigorieva, C. Schönenberger, P. Seneor, C. Stampfer, S. O. Valenzuela, X. Waintal, and B. van Wees, *2D Mater.* **2**, 030202 (2015).
- [13] M. V. Kamalakar, A. Dankert, J. Bergsten, T. Ive, and S. P. Dash, *Appl. Phys. Lett.* **105**, 212405 (2014).
- [14] M. Gurram, S. Omar, and B. J. van Wees, *2D Materials* **5**, 032004 (2018).
- [15] M. H. D. Guimarães, P. J. Zomer, J. Ingla-Aynés, J. C. Brant, N. Tombros, and B. J. van Wees, *Physical Review Letters* **113**, 086602 (2014).
- [16] S. Singh, J. Katoch, J. Xu, C. Tan, T. Zhu, W. Amamou, J. Hone, and R. Kawakami, *Applied Physics Letters* **109** (2016), 10.1063/1.4962635.
- [17] M. Drögeler, C. Franzen, F. Volmer, T. Pohlmann, L. Banszerus, M. Wolter, K. Watanabe, T. Taniguchi, C. Stampfer, and B. Beschoten, *Nano Letters* **16**, 3533 (2016).
- [18] M. Drögeler, F. Volmer, C. Stampfer, and B. Beschoten, *Physica Status Solidi (B) Basic Research* **254**, 1 (2017).
- [19] P. J. Zomer, M. H. D. Guimarães, N. Tombros, and B. J. van Wees, *Phys. Rev. B* **86**, 161416 (2012).
- [20] J. Ingla-Aynés, M. H. D. Guimarães, R. J. Meijerink, P. J. Zomer, and B. J. van Wees, *Phys. Rev. B* **92**, 201410 (2015).
- [21] M. Drögeler, F. Volmer, M. Wolter, B. Terrés, K. Watanabe, T. Taniguchi, G. Güntherodt, C. Stampfer, and B. Beschoten, *Nano Lett.* **14**, 6050 (2014).
- [22] C. Dean, A. Young, L. Wang, I. Meric, G.-H. Lee, K. Watanabe, T. Taniguchi, K. Shepard, P. Kim, and J. Hone, *Solid State Commun.* **152**, 1275 (2012).
- [23] C. R. Dean, A. F. Young, I. Meric, C. Lee, L. Wang, S. Sorgenfrei, K. Watanabe, T. Taniguchi, P. Kim, K. L. Shepard, and J. Hone, *Nat. Nanotechnol.* **5**, 722 (2010).
- [24] J. Wang, F. Ma, and M. Sun, *RSC Adv.* **7**, 16801 (2017).
- [25] L. Banszerus, M. Schmitz, S. Engels, J. Dauber, M. Oellers, F. Haupt, K. Watanabe, T. Taniguchi, B. Beschoten, and C. Stampfer, *Sci. Adv.* **1**, 1 (2015).
- [26] N. Petrone, C. R. Dean, I. Meric, A. M. Van Der Zande, P. Y. Huang, L. Wang, D. Muller, K. L. Shepard, and J. Hone, *Nano Lett.* **12**, 2751 (2012).
- [27] V. E. Calado, S. E. Zhu, S. Goswami, Q. Xu, K. Watanabe, T. Taniguchi, G. C. Janssen, and L. M. Vander-sypen, *Appl. Phys. Lett.* **104** (2014), 10.1063/1.4861627.
- [28] J. C. Leutenantsmeyer, J. Ingla-Aynés, J. Fabian, and B. J. van Wees, *Phys. Rev. Lett.* **121**, 127702 (2018).
- [29] J. Xu, T. Zhu, Y. K. Luo, Y.-M. Lu, and R. K. Kawakami, *Phys. Rev. Lett.* **121**, 127703 (2018).
- [30] A. W. Cummings, J. H. Garcia, J. Fabian, and S. Roche, *Phys. Rev. Lett.* **119**, 206601 (2017).
- [31] S. Zihlmann, A. W. Cummings, J. H. Garcia, M. Kedves, K. Watanabe, T. Taniguchi, C. Schönenberger, and P. Makk, *Phys. Rev. B* **97**, 075434 (2018).
- [32] S. Omar and B. J. van Wees, *Phys. Rev. B* **97**, 045414 (2018).
- [33] M. Gmitra, D. Kochan, P. Högl, and J. Fabian, *Phys. Rev. B* **93**, 155104 (2016).
- [34] M. Gmitra, S. Konschuh, C. Ertler, C. Ambrosch-Draxl, and J. Fabian, *Phys. Rev. B* **80**, 235431 (2009).
- [35] S. Konschuh, M. Gmitra, D. Kochan, and J. Fabian, *Phys. Rev. B* **85**, 115423 (2012).
- [36] D. Van Tuan, F. Ortman, A. W. Cummings, D. Soriano, and S. Roche, *Scientific Reports* **6**, 1 (2016).
- [37] J. Jung, A. Raoux, Z. Qiao, and A. H. MacDonald, *Phys.*

- Rev. B **89**, 205414 (2014).
- [38] P. Moon and M. Koshino, Phys. Rev. B **90**, 155406 (2014).
 - [39] G. Argentero, A. Mittelberger, M. Reza Ahmadpour Monazam, Y. Cao, T. J. Pennycook, C. Mangler, C. Kramberger, J. Kotakoski, A. K. Geim, and J. C. Meyer, Nano Letters **17**, 1409 (2017).
 - [40] R. Quhe, J. Zheng, G. Luo, Q. Liu, R. Qin, J. Zhou, D. Yu, S. Nagase, W. N. Mei, Z. Gao, and J. Lu, NPG Asia Materials **4**, 1 (2012).
 - [41] G. Giovannetti, P. A. Khomyakov, G. Brocks, P. J. Kelly, and J. Van Den Brink, Physical Review B **76**, 073103 (2007).
 - [42] See Supplemental Material for further information about the computational details, fitting results for graphene/hBN heterostructures considering different stacking configurations including a distance study, as well as the influence of a transverse electric field. We also show calculated spin-orbit fields, analyze the atomic contributions to the spin-orbit splittings and show further results on spin relaxation anisotropy for graphene on hBN.
 - [43] D. Kochan, S. Imer, and J. Fabian, Phys. Rev. B **95**, 165415 (2017).

Supplemental Material:

Field-controllable giant spin relaxation anisotropy in (hBN)/graphene/hBN heterostructures

Klaus Zollner,^{1,*} Martin Gmitra,² and Jaroslav Fabian¹

¹*Institute for Theoretical Physics, University of Regensburg, 93040 Regensburg, Germany*

²*Institute of Physics, P. J. Šafárik University in Košice, 04001 Košice, Slovakia*

The supplemental material contains further information about graphene on hBN, as well as hBN encapsulated graphene. We include a description of the computational details. In the case of graphene on hBN we show the fitting results for the three high-symmetry stacking configurations and discuss, where possible discrepancies between the first-principles data and the model Hamiltonian come from, by analyzing atomic contributions to the spin-orbit band splitting. Further, we study how the fitted parameters depend on the distance and we show the calculated spin-orbit vector fields and spin-orbit splittings of the bands, for graphene on hBN, around the K point. We also include a brief discussion about a low-symmetry stacking case of graphene/hBN. For the lowest energy configuration of graphene on hBN, we show how the parameters depend on a transverse electric field. In the case of hBN encapsulated graphene, we show further fitting results for few different stacking configurations. Finally, we show how we calculate spin relaxation times and anisotropies and present further results on anisotropies for graphene/hBN.

COMPUTATIONAL DETAILS

First-principles calculations are performed with full potential linearized augmented plane wave (FLAPW) code based on density functional theory (DFT) and implemented in WIEN2k [1]. Exchange-correlation effects are treated with the generalized-gradient approximation (GGA) [2], including dispersion correction [3] and using a k -point grid of $42 \times 42 \times 1$ in the hexagonal Brillouin-Zone if not specified otherwise. The values of the Muffin-tin radii we use are $r_C = 1.34$ for C atom, $r_B = 1.27$ for B atom, and $r_N = 1.40$ for N atom. We use the plane wave cutoff parameter $R_{KMAX} = 9.5$. In order to calculate the band structure of graphene/hBN heterostructures, we use a common unit cell for graphene and hBN. Therefore we fix the lattice constant of graphene [4] to $a = 2.46 \text{ \AA}$, and change the hBN lattice constant, from its experimental value [5] of $a = 2.504 \text{ \AA}$, to the graphene one. The stacking of graphene on hBN is also a crucial point, however it was already shown that the configuration with the lowest energy is, when one C atom is over the B atom and the other C atom is over the hollow site of hBN [6]. Defining the positions of hBN as B

(Boron), N (Nitrogen), and H (hollow site at center of the hexagon), and the two graphene sublattices α (C_A) and β (C_B), we call the energetically most favorable configuration ($\alpha B, \beta H$), where C_A is over Boron, and C_B is over the hollow site. According to this definition we define the other configurations as ($\alpha N, \beta H$) and ($\alpha N, \beta B$). In principle the relaxed distances between graphene and hBN are different for the different stackings [6]. However, a distance study for all three configurations, reveals what is the lowest energy distance. In order to avoid interactions between periodic images of our slab geometry, we add a vacuum of at least 20 \AA in z-direction.

GRAPHENE ON HBN

In Fig. S1 we show the calculated low energy band structure in the vicinity of the K point with a fit to our minimal tight-binding Hamiltonian \mathcal{H} for ($\alpha B, \beta H$) configuration of graphene on hBN.

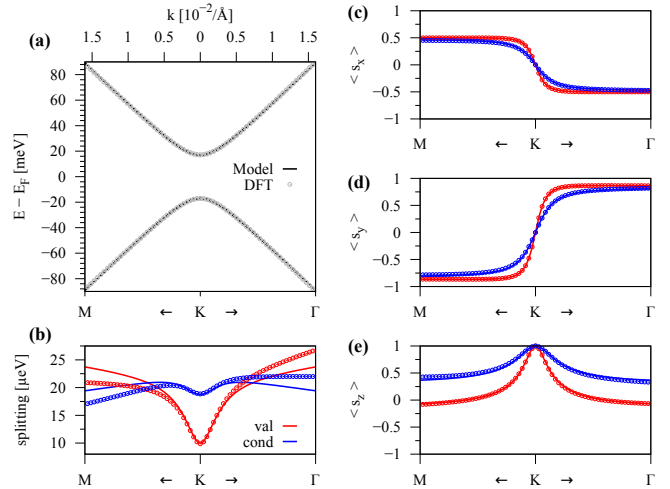


FIG. S1. (Color online) Calculated band properties of graphene on hBN in the vicinity of the K point for ($\alpha B, \beta H$) configuration and an interlayer distance of 3.35 \AA . (a) First-principles band structure (symbols) with a fit to the model Hamiltonian (solid line). (b) The splitting of conduction band ΔE_{CB} (blue) and valence band ΔE_{VB} (red) close to the K point and calculated model results. (c)-(e) The spin expectation values of the bands ε_2^{VB} and ε_1^{CB} and comparison to the model results. The fit parameters are given in the main text.

We can see that the orbital band structure is perfectly

reproduced by our model, see Fig. S1(a). The splittings of the bands are shown in Fig. S1(b), which are in the μeV range and are defined as $\Delta E_{\text{CB}} = \varepsilon_2^{\text{CB}} - \varepsilon_1^{\text{CB}}$ and $\Delta E_{\text{VB}} = \varepsilon_2^{\text{VB}} - \varepsilon_1^{\text{VB}}$. Also the splittings are nicely reproduced by the model, with a maximum discrepancy of about 10% compared to the first-principles data. More specifically, the splittings are overestimated (underestimated) along the K-M (K- Γ) path, by the model. Finally, Fig. S1(c)-(e) show the spin expectation values of the bands $\varepsilon_2^{\text{VB}}$ and $\varepsilon_1^{\text{CB}}$, which are in perfect agreement with the model.

In Fig. S2 we show the calculated dispersion as a 2D-map in k_x - k_y -plane in the vicinity of the K point for the (αB , βH) configuration. The energies of the bands,

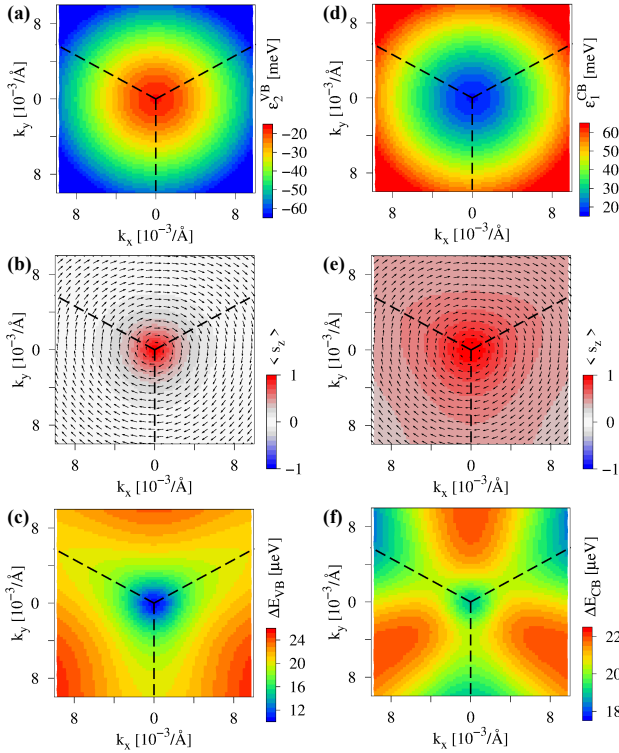


FIG. S2. (Color online) Calculated low energy dispersion of graphene on hBN around K point for (αB , βH) configuration and an interlayer distance of 3.35 Å. (a) 2D-map of the energy of the valence band $\varepsilon_2^{\text{VB}}$, with the corresponding spin texture of the band shown in (b) and the splitting of the valence band $\Delta E_{\text{VB}} = \varepsilon_2^{\text{VB}} - \varepsilon_1^{\text{VB}}$ shown in (c). (d)-(f) The same as (a)-(c), but for conduction band $\varepsilon_1^{\text{CB}}$ and conduction band splitting $\Delta E_{\text{CB}} = \varepsilon_2^{\text{CB}} - \varepsilon_1^{\text{CB}}$. The dashed lines show the edges of the Brillouin Zone with the K point at the center.

$\varepsilon_2^{\text{VB}}$ and $\varepsilon_1^{\text{CB}}$, do not show any trigonal warping, see Fig. S2(a,d). However already the spin texture shows that trigonal warping is present with a very pronounced Rashba spin-orbit field, see Fig. S2(b,e), as expected from the inversion symmetry breaking by the hBN substrate. A pronounced threefold symmetry is observed in the spin splittings ΔE_{VB} and ΔE_{CB} , see Fig. S2(c,f).

In this case, our model Hamiltonian agrees very good on a qualitative level, however the very fine details cannot be captured by the model. The reason will be explained later on.

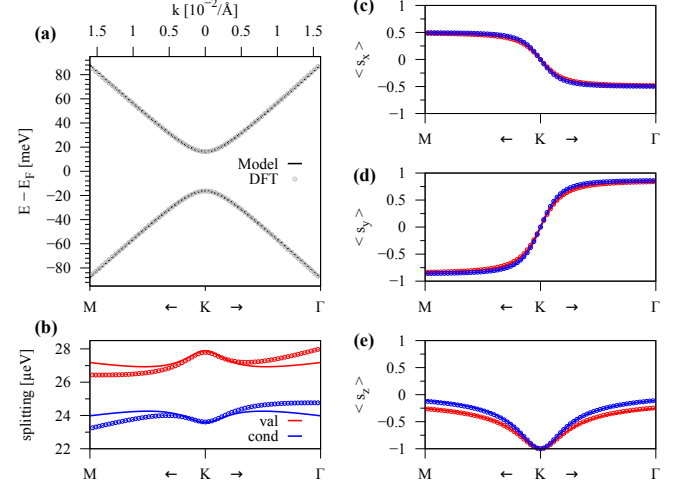


FIG. S3. (Color online) Calculated band properties of graphene on hBN in the vicinity of the K point for (αN , βH) configuration and an interlayer distance of 3.50 Å. (a) First-principles band structure (symbols) with a fit to the model Hamiltonian (solid line). (b) The splitting of conduction band ΔE_{CB} (blue) and valence band ΔE_{VB} (red) close to the K point and calculated model results. (c)-(e) The spin expectation values of the bands $\varepsilon_2^{\text{VB}}$ and $\varepsilon_1^{\text{CB}}$ and comparison to the model results. The fit parameters are given in the main text.

Also for the other high-symmetry stacking configurations, we find that the model Hamiltonian agrees very well with the first-principles data. In Figs. S3 and S4 we show the fit to the model Hamiltonian for the (αN , βH) and (αN , βB) configurations. The overall results look quite similar to the (αB , βH) configuration, however the s_z -expectation values are opposite in these cases, compared to (αB , βH) case. Also the splittings are much better reproduced in these two cases, with a maximum discrepancy of 3% and 1%, respectively. The spin expectation values are perfectly reproduced by the model. We find that our model is very robust and different stacking configurations are described by different parameter sets.

In Figs. S5 and S6 we show the calculated dispersion as a 2D-map in k_x - k_y -plane in the vicinity of the K point for the (αN , βH) and (αN , βB) configurations. The overall trigonal symmetry features remain and are very similar to (αB , βH) configuration.

One also has to mention that different stacking configurations lead to different distances between graphene and hBN. In Fig. S7 we show the fitting parameters as a function of the distance between graphene and hBN and for the three stacking configurations. We find that the total energy is lowest for the (αB , βH) configuration with an interlayer distance of 3.35 Å, see Fig. S7(a). The lowest energy for the (αN , βH) and (αN , βB) configura-

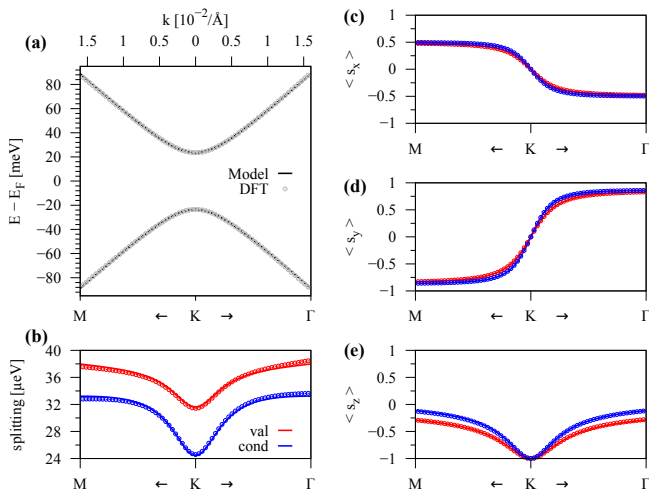


FIG. S4. (Color online) Calculated band properties of graphene on hBN in the vicinity of the K point for $(\alpha N, \beta B)$ configuration and an interlayer distance of 3.55 \AA . (a) First-principles band structure (symbols) with a fit to the model Hamiltonian (solid line). (b) The splitting of conduction band ΔE_{CB} (blue) and valence band ΔE_{VB} (red) close to the K point and calculated model results. (c)-(e) The spin expectation values of the bands ε_2^{VB} and ε_1^{CB} and comparison to the model results. The fit parameters are given in the main text.

tions are obtained at a distance of 3.50 \AA and 3.55 \AA . The Fermi velocity v_F , see Fig. S7(b), which reflects the nearest neighbor hopping strength via $t = \frac{2\hbar v_F}{\sqrt{3}a}$, grows as a function of distance, especially for the $(\alpha N, \beta H)$ and $(\alpha N, \beta B)$ configurations. In contrast to that, the gap parameter Δ decreases with distance, in agreement with literature [6]. When moving the graphene away from the substrate, the sublattice symmetry breaking reduces and thus the gap decreases.

One very important observation is that the gap parameter Δ of the $(\alpha B, \beta H)$ configuration is opposite in sign compared to the other configurations, as seen in a moiré-pattern [7]. In the $(\alpha B, \beta H)$ configuration, the C_A sublattice is over the Boron. Sublattice C_A forms, in this case, the valence band which is why we need a negative value of Δ in the model. In contrast, the other configurations have the C_A sublattice over the Nitrogen, which then forms the conduction band, leading to positive value of Δ . This also explains, why the s_z -expectation values for different configurations are different, compare Figs. S1(e) and S3(e).

In a moiré-pattern, as already mentioned, all stacking configurations can appear. Consequently, there could be a local stacking geometry where the orbital gap closes, appearing when the two sublattices feel the same surrounding potential.

The Rashba SOC parameter, see Fig. S7(d), also decreases with distance. As the distance between graphene and hBN goes to infinity, the inversion symmetry of graphene is restored and the Rashba SOC parameter van-

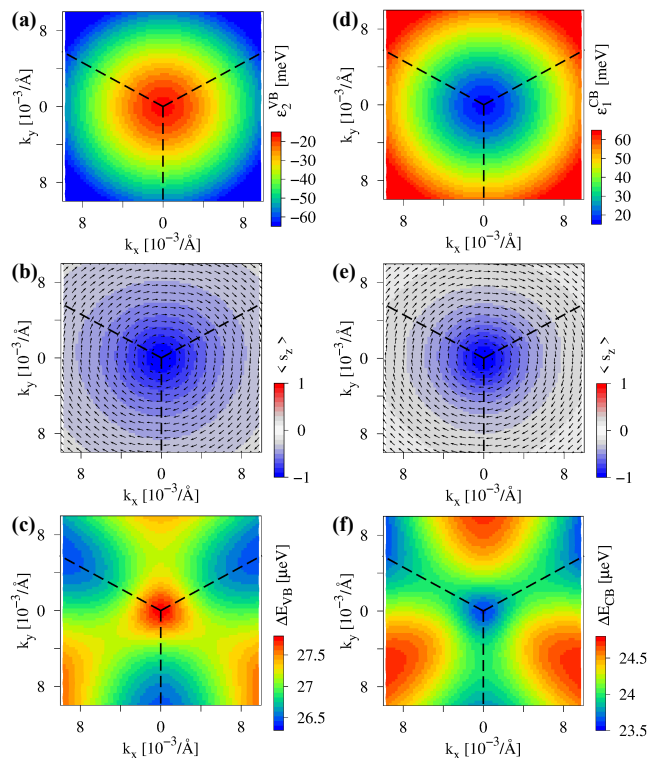


FIG. S5. (Color online) Calculated low energy dispersion of graphene on hBN around K point for $(\alpha N, \beta H)$ configuration and an interlayer distance of 3.50 \AA . (a) 2D-map of the energy of the valence band ε_2^{VB} , with the corresponding spin texture of the band shown in (b) and the splitting of the valence band $\Delta E_{VB} = \varepsilon_2^{VB} - \varepsilon_1^{VB}$ shown in (c). (d)-(f) The same as (a)-(c), but for conduction band ε_1^{CB} and conduction band splitting $\Delta E_{CB} = \varepsilon_2^{CB} - \varepsilon_1^{CB}$. The dashed lines show the edges of the Brillouin Zone with the K point at the center.

ishes. The two intrinsic SOC parameters λ_1^A and λ_1^B approach the intrinsic SOC parameter of $12 \mu\text{eV}$ of pristine graphene [8], as we increase the distance, see Fig. S7(e,f). Finally we find that the two PIA SOC parameters λ_{PIA}^A and λ_{PIA}^B also decrease with distance, see Fig. S7(g,h).

We now want to clarify two remaining issues: (i) Where does the discrepancy between the model and the first-principles data, see Fig. S1(b), come from? (ii) Is there a low-symmetry stacking configuration, where the orbital gap closes?

In the case of $(\alpha B, \beta H)$ configuration we have found that, the splittings are overestimated (underestimated) along the K-M (K- Γ) path, by the model. The discrepancy in the splitting of the bands is due to the influence of the substrate. In general the model Hamiltonian \mathcal{H} just considers effective π -orbitals of graphene, however there seems to be a subtle influence from a hybridization to the p -orbitals of hBN. If we look at the Density of States (DOS) for the $(\alpha B, \beta H)$ case, see Fig. S8, we find that close to the Dirac point there is a small contribution from Nitrogen and Boron p -states. Especially Boron

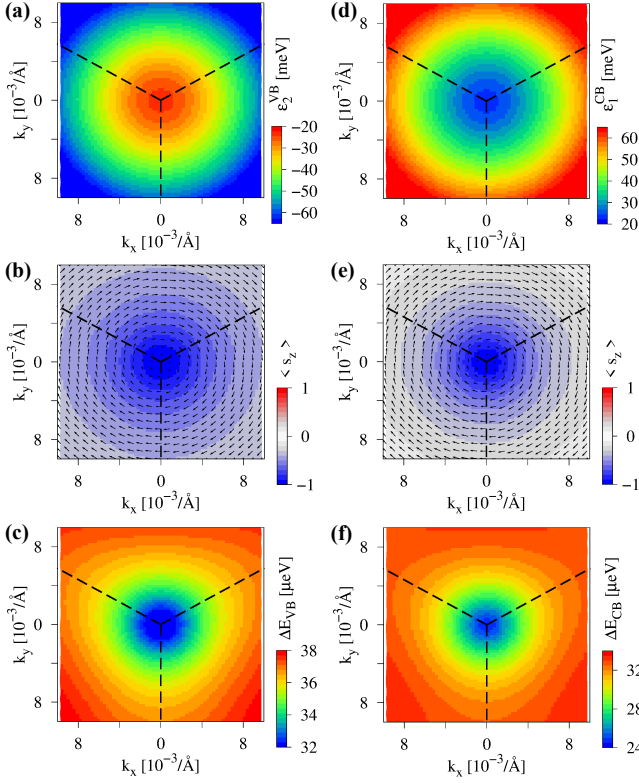


FIG. S6. (Color online) Calculated low energy dispersion of graphene on hBN around K point for $(\alpha N, \beta B)$ configuration and an interlayer distance of 3.55 Å. (a) 2D-map of the energy of the valence band ε_2^{VB} , with the corresponding spin texture of the band shown in (b) and the splitting of the valence band $\Delta E_{VB} = \varepsilon_2^{VB} - \varepsilon_1^{VB}$ shown in (c). (d)-(f) The same as (a)-(c), but for conduction band ε_1^{CB} and conduction band splitting $\Delta E_{CB} = \varepsilon_2^{CB} - \varepsilon_1^{CB}$. The dashed lines show the edges of the Brillouin Zone with the K point at the center.

p_z -orbitals and Nitrogen $p_x + p_y$ -orbitals are contributing close to the charge neutrality point.

Moreover, from our distance study we find that the discrepancy between the model and the first-principles data is getting smaller as we increase the distance. Finally, we calculated the low energy band structures, when SOC is artificially turned off on the Nitrogen, Boron, or Carbon atoms, respectively. The fit parameters for these situations are given in Tab. S1, along with the maximum discrepancy for each situation. We find a severe improvement of the fit, when SOC of the Nitrogen atom is turned off. Especially, if we turn off SOC on the Carbon atoms of graphene, we find negative intrinsic SOC parameters λ_1^A and λ_1^B . Thus Nitrogen gives a negative contribution to the SOC splitting of the Dirac bands.

Combining the DOS, the band splittings and the fit parameters, when SOC is turned off, we conclude that the discrepancy comes from Nitrogen $p_x + p_y$ -orbitals, that hybridize with π -orbitals of graphene. Already such a very small contribution of $p_x + p_y$ -orbitals, see Fig. S8(a),

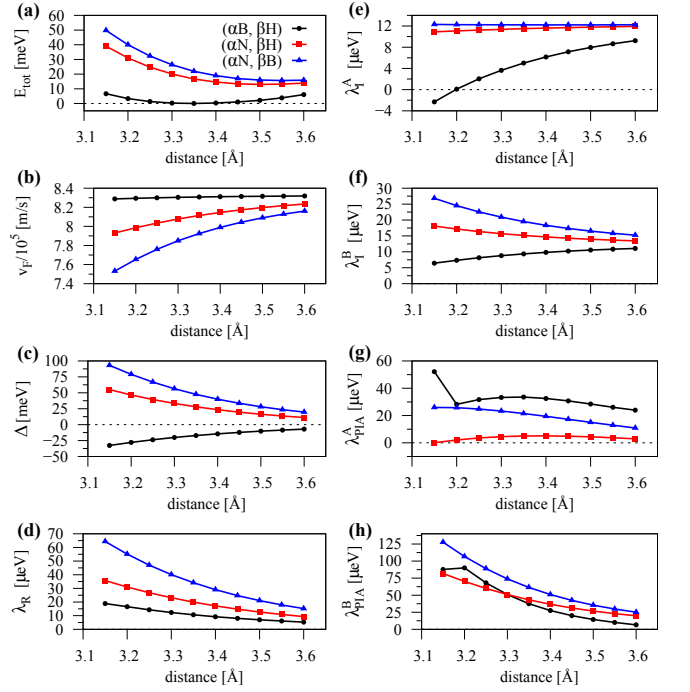


FIG. S7. (Color online) Fit parameters as a function of distance between graphene and hBN for the three different stacking configurations. (a) Total energy, (b) the Fermi velocity v_F , (c) gap parameter Δ , (d) Rashba SOC parameter λ_R , (e) intrinsic SOC parameter λ_1^A for sublattice A, (f) intrinsic SOC parameter λ_1^B for sublattice B, (g) PIA SOC parameter λ_{PIA}^A for sublattice A, and (h) PIA SOC parameter λ_{PIA}^B for sublattice B.

can substantially influence the spin splitting and an effective model based only on π -orbitals of graphene can no longer perfectly describe the results. However, the overall fit is still very good and sufficient for our needs.

We have seen, that different stackings can lead to a different sign of the gap parameter Δ . Consequently, as already mentioned, a certain local stacking geometry could have a closed orbital gap. In Fig. S9 we show the low energy band properties of an arbitrary stacking geometry, without having any symmetry [9]. First of all, we notice that the Dirac point is no longer located at the K point. From the corresponding geometry in Fig. S9(a), we find that the hoppings, from say C_A to the three nearest neighbors C_B , are all different due to the substrate. This asymmetry in the nearest neighbor hopping amplitudes leads to the shift of the Dirac point in momentum space [10, 11]. Since our model Hamiltonian considers only high-symmetry stacking configurations, without shifted Dirac cone, we also cannot fit the data with it. From the spin expectation values we find a very pronounced Rashba spin-orbit field, as the s_z -component is strongly suppressed. In order to identify the location of the Dirac point in momentum space, we calculated the dispersion as a 2D-map in k_x - k_y -plane

SOC on	$v_F/10^5 [\frac{m}{s}]$	Δ [meV]	λ_R [μeV]	λ_I^A [μeV]	λ_I^B [μeV]	λ_{PIA}^A [μeV]	λ_{PIA}^B [μeV]	discr. [a.u.]
N, B, C	8.308	-17.08	10.65	5.00	9.37	33.58	37.57	1.265
N, C	8.308	-17.08	12.22	5.01	8.95	34.65	34.82	1.269
B, C	8.308	-17.08	10.23	12.08	12.66	-0.06	-34.82	0.260
N, B	8.308	-17.07	-1.82	-7.09	-2.79	-9.53	66.55	1.349
C	8.308	-17.07	11.85	12.07	12.25	-4.60	-32.67	0.268

TABLE S1. Summary of the fitting parameters of Hamiltonian \mathcal{H} , for graphene on hBN for (αB , βH) configuration and an interlayer distance of 3.35 Å. Here, we have artificially turned off SOC on Nitrogen, Boron, or Carbon atoms, respectively. The Fermi velocity v_F , gap parameter Δ , Rashba SOC parameter λ_R , intrinsic SOC parameters λ_I^A and λ_I^B for sublattice A and B, and PIA SOC parameters λ_{PIA}^A and λ_{PIA}^B for sublattice A and B. The discrepancy is the calculated residual of the fit along the M-K- Γ path given in arbitrary units.

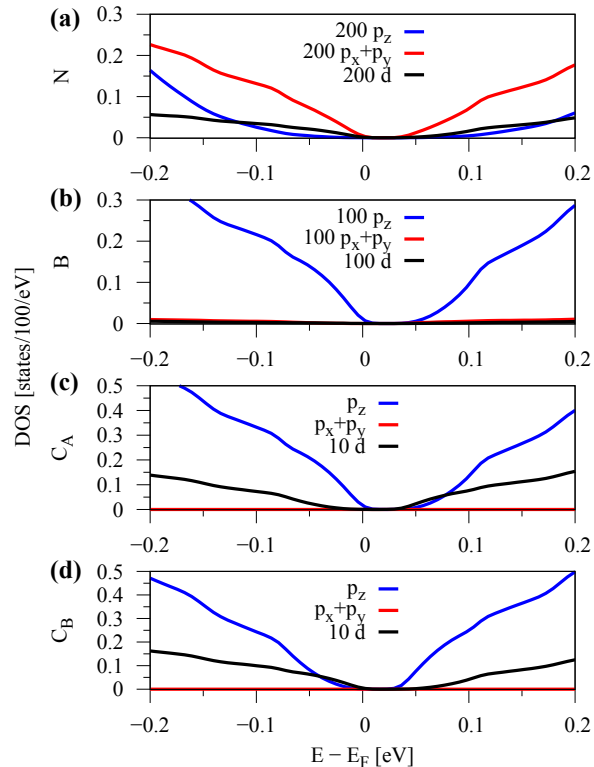


FIG. S8. (Color online) Density of states of graphene on hBN around the Fermi level for (αB , βH) configuration and an interlayer distance of 3.35 Å. The DOS is multiplied by a factor of 100. Each subfigure (a)-(d) correspond to a different atom. For each atom, the orbital contributions to the DOS are multiplied with the corresponding prefactor. The DOS is calculated with a k -point grid of $180 \times 180 \times 1$.

in the vicinity of the K point, see Fig. S10. We can see that the Dirac point is shifted away from the corner of the Brillouin zone. At this "new" K point, the orbital gap is 1.64 meV large. Due to the limited number of k -points in the calculation grid for the 2D-map, we cannot identify the exact position of the Dirac point, so the orbital gap is not fully closed, but much smaller than in the high-symmetry stacking cases. We also notice that the spin-orbit field is almost purely in-plane without

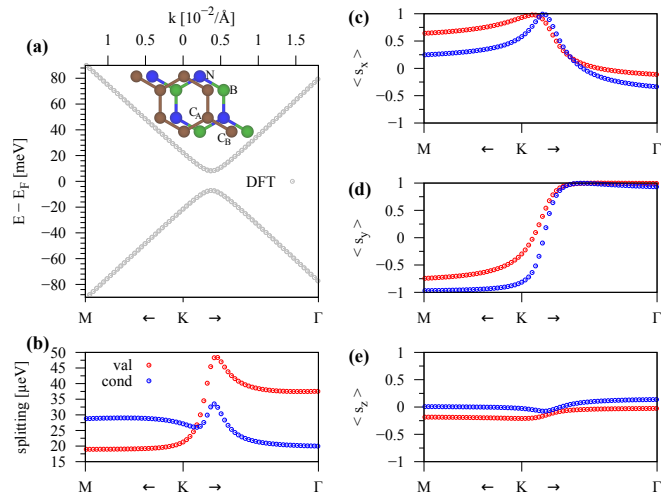


FIG. S9. (Color online) Calculated band properties of graphene on hBN in the vicinity of the K point and an interlayer distance of 3.45 Å. (a) First-principles band structure and local stacking geometry. (b) The splitting of conduction band ΔE_{CB} (blue) and valence band ΔE_{VB} (red) close to the K point. (c)-(e) The spin expectation values of the bands $\varepsilon_2^{\text{VB}}$ and $\varepsilon_1^{\text{CB}}$.

any s_z -component, see Fig. S10(b,e), in a very large area around the Dirac point. Consequently Rashba SOC plays an important role in this low-symmetry stacking configuration. Especially if we look at the spin-orbit splitting of the bands, Fig. S10(c,f), we find that there is no trigonal symmetry remaining. Different paths in the Brillouin zone are no longer connected by symmetry. Such a stacking configuration completely breaks the symmetry of the graphene, due to the different hopping amplitudes between nearest neighbors caused by the hBN substrate. Of course, in a moiré-pattern, several other stackings are present that lead to very different local spin-orbit fields.

HBN ENCAPSULATED GRAPHENE

From our previous study of graphene on hBN, we already know what is the energetically most favorable

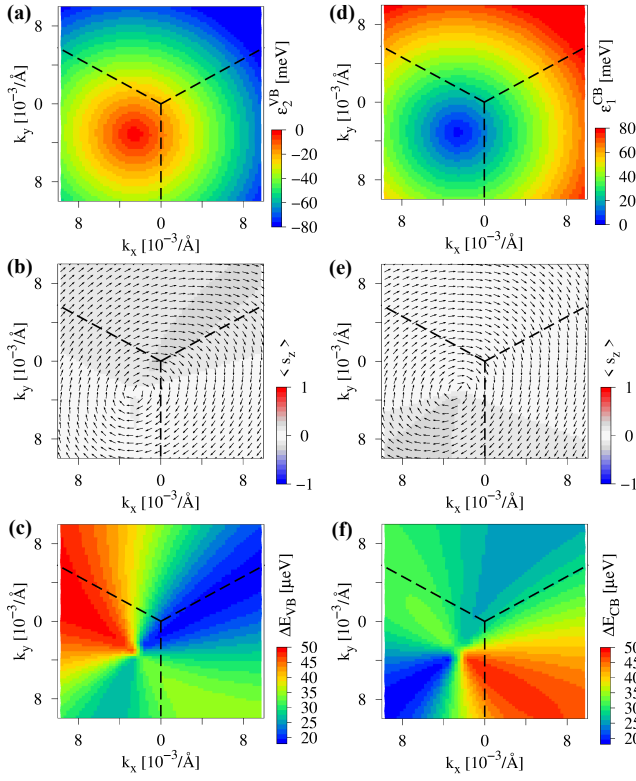


FIG. S10. (Color online) Calculated low energy dispersion of graphene on hBN around K point for stacking configuration in Fig. S9 and an interlayer distance of 3.45 Å. (a) 2D-map of the energy of the valence band $\varepsilon_2^{\text{VB}}$, with the corresponding spin texture of the band shown in (b) and the splitting of the valence band $\Delta E_{\text{VB}} = \varepsilon_2^{\text{VB}} - \varepsilon_1^{\text{VB}}$ shown in (c). (d)-(f) The same as (a)-(c), but for conduction band $\varepsilon_1^{\text{CB}}$ and conduction band splitting $\Delta E_{\text{CB}} = \varepsilon_2^{\text{CB}} - \varepsilon_1^{\text{CB}}$. The dashed lines show the edges of the Brillouin Zone with the K point at the center.

distance for each stacking geometry, which we keep for the encapsulated cases, respectively. Depending on the stacking of the top and bottom hBN with respect to the graphene, different interlayer distances can be present. We define the stacking sequences in analogy to the graphene on hBN case, for example, the energetically most favorable configuration is then (H α H, B β B), which is the C1-configuration of the main text. According to this, we define several other configurations.

For such a configuration, like (H α H, B β B), we recover the mirror symmetry of graphene, and thus we arrive at the D_{3h} subgroup. From Ref. 12, we know that the only SOC terms left are $\lambda_{\Gamma}^{\text{A}}$ and $\lambda_{\Gamma}^{\text{B}}$, while λ_{R} , $\lambda_{\text{P1A}}^{\text{A}}$ and $\lambda_{\text{P1A}}^{\text{B}}$ are forbidden by symmetry. For the (H α B, B β H) configuration we recover the inversion symmetry and arrive at the D_{3d} subgroup. In this case we have the two Carbon sublattices equal and $\Delta = 0$, $\lambda_{\Gamma}^{\text{A}} = \lambda_{\Gamma}^{\text{B}}$, $\lambda_{\text{R}} = 0$, and $\lambda_{\text{P1A}}^{\text{A}} = \lambda_{\text{P1A}}^{\text{B}}$ must hold.

In Fig. S11, we show the low energy band properties of the C1-configuration, along with a fit to our model

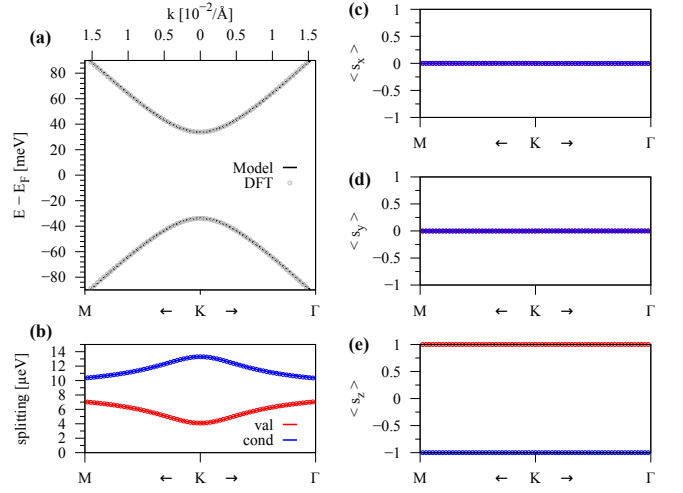


FIG. S11. (Color online) Calculated band properties of hBN encapsulated graphene in the vicinity of the K point for C1-configuration and interlayer distances of 3.35 Å between graphene and the hBN layers without external electric field. (a) First-principles band structure (symbols) with a fit to the model Hamiltonian (solid line). (b) The splitting of conduction band ΔE_{CB} (blue) and valence band ΔE_{VB} (red) close to the K point and calculated model results. (c)-(e) The spin expectation values of the bands $\varepsilon_2^{\text{VB}}$ and $\varepsilon_1^{\text{CB}}$ and comparison to the model results. The fit parameters are given in the main text.

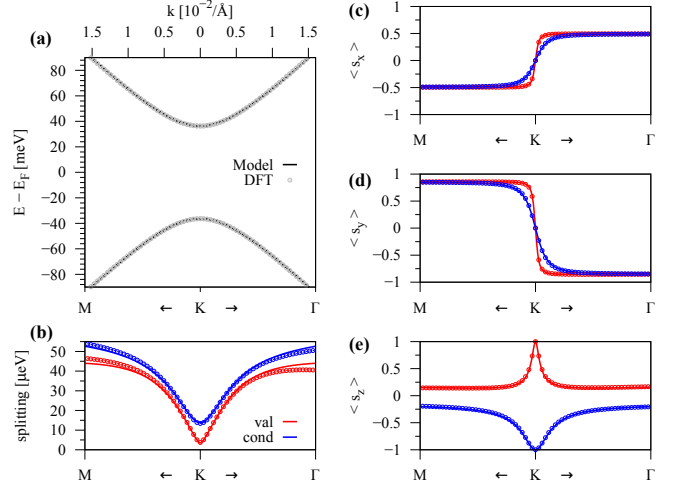


FIG. S12. (Color online) Calculated band properties of hBN encapsulated graphene in the vicinity of the K point for C1-configuration and interlayer distances of 3.35 Å between graphene and the hBN layers with external electric field of 5 V/nm. (a) First-principles band structure (symbols) with a fit to the model Hamiltonian (solid line). (b) The splitting of conduction band ΔE_{CB} (blue) and valence band ΔE_{VB} (red) close to the K point and calculated model results. (c)-(e) The spin expectation values of the bands $\varepsilon_2^{\text{VB}}$ and $\varepsilon_1^{\text{CB}}$ and comparison to the model results. The fit parameters are given in the main text.

Hamiltonian without any applied external electric field. We can see perfect agreement with the first-principles

data, just using the four parameters v_F , Δ , λ_I^A , and λ_I^B . Rashba and PIA SOC parameters are not necessary and strictly zero for the fit, especially for this mirror symmetric configuration, as explained. Therefore the bands are purely s_z -polarized.

In Fig. S12 we show the low energy band properties of the C1-configuration, along with a fit to our model Hamiltonian with applied external electric field of 5 V/nm. Comparing the two results, Figs. S11 and S12, we can clearly see that the orbital low energy band structure looks the very same. However, the band splittings away from the K point are strongly enhanced and the spin expectation values show a clear signature of Rashba SOC. The application of a realistic electric field of 5 V/nm enhances the spin-orbit band splittings by a factor of 5 away from the K point, compare Figs. S11 and S12. This has substantial influence on the spin lifetime and anisotropy, as we show in the main text.

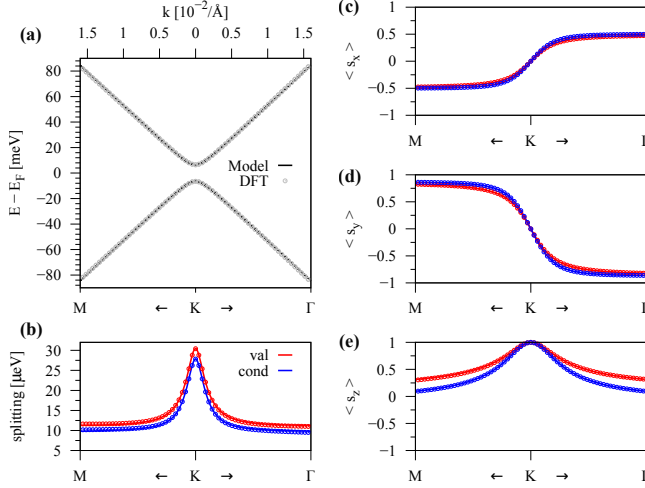


FIG. S13. (Color online) Calculated band properties of hBN encapsulated graphene in the vicinity of the K point for (BaN, NβH) configuration with a distance of 3.55 Å (3.50 Å) between graphene and the top (bottom) hBN layer. (a) First-principles band structure (symbols) with a fit to the model Hamiltonian (solid line). (b) The splitting of conduction band ΔE_{CB} (blue) and valence band ΔE_{VB} (red) close to the K point and calculated model results. (c)-(e) The spin expectation values of the bands ε_2^{VB} and ε_1^{CB} and comparison to the model results. The fit parameters are given in the main text.

In Figs. S13 and S14, we show the low energy band properties of the (BaN, NβH) and (NaN, BβH) configurations, along with a fit to our model Hamiltonian, as further examples of the robustness of the Hamiltonian. We can see again perfect agreement with the first-principles data. It is quite interesting that for this case, as well as for other hBN encapsulated configurations, the Rashba SOC parameter is negative. This means that the spin-orbit field rotates in the counter-clockwise direction, in contrast to the graphene/hBN cases, see for example Fig. S2.

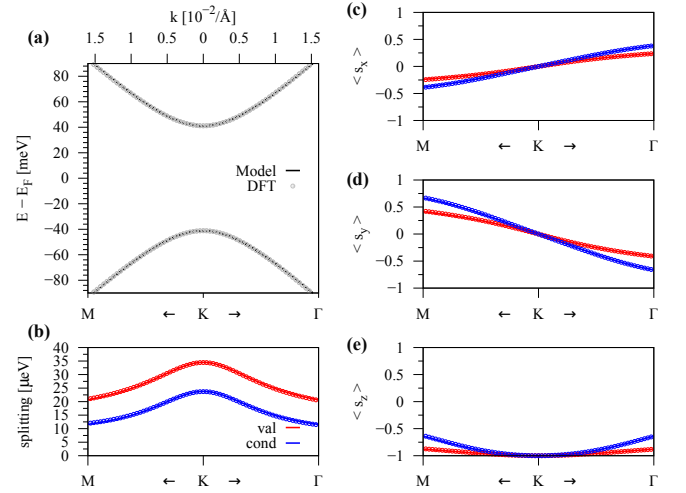


FIG. S14. (Color online) Calculated band properties of hBN encapsulated graphene in the vicinity of the K point for (NaN, BβH) configuration with a distance of 3.55 Å (3.50 Å) between graphene and the top (bottom) hBN layer. (a) First-principles band structure (symbols) with a fit to the model Hamiltonian (solid line). (b) The splitting of conduction band ΔE_{CB} (blue) and valence band ΔE_{VB} (red) close to the K point and calculated model results. (c)-(e) The spin expectation values of the bands ε_2^{VB} and ε_1^{CB} and comparison to the model results. The fit parameters are given in the main text.

In a similar way, we calculate the dispersion and fit it to our model, for other configurations of hBN encapsulated graphene. We summarize the results in the main text. We find that there is another configuration, (HαB, BβH), having almost the same low energy as the (HαH, BβB) one, in agreement with literature [13]. Similarly, we only get the by symmetry allowed parameters, as for all other configurations. In real systems, one expects that all of these configurations are present at the same time, due to the moiré-pattern that is formed as a consequence of slightly different lattice constants of graphene and hBN. In addition stacking configurations can occur that, locally, have no symmetry at all, as shown in the previous section, making these heterostructures quite complicated to describe on the global scale. What is also interesting to note is that the configurations with $\Delta = 0$ have $\lambda_I^A = \lambda_I^B = \lambda_I$, so the spectrum opens a gap due to SOC with degenerate conduction and valence band. It is also worth to notice that if one looks for example at the (HαH, BβB) configuration and take the average of λ_I^A and λ_I^B you arrive at the parameter λ_I for the (HαB, BβH) configuration.

In real experiments, also asymmetric hBN encapsulated graphene structures are used, say with two hBN layers below graphene and one hBN layer above it. We also calculate this scenario, especially for the configurations that are energetically most favorable. The stacking of hBN itself is (BN, NB) (Boron over Nitrogen, Nitrogen over Boron) and we take a distance of 3.35 Å between the

hBN layers. These configurations and their fit parameters are also summarized in the main text, with the naming convention in analogy to the other cases. Comparing the results of this asymmetric encapsulations with the corresponding symmetric encapsulations — for example compare (H α H, B β B) and (B α BN, H β HH) — we find that they are almost the same. The only thing is that the C_A and C_B sublattice are interchanged in these two configurations, which is also reflected in the parameters.

One of the main conclusions is that in the case of hBN encapsulated graphene, the average Rashba SOC parameter is reduced in contrast to the graphene/hBN average Rashba parameter, while intrinsic SOC parameters have similar magnitudes. Therefore, in spin transport, hBN encapsulated graphene should lead to longer spin relaxation times for out-of-plane spins.

TRANSVERSE ELECTRIC FIELD

In experiment usually gating is required to tune the Fermi level towards the charge neutrality point. Thereby the transverse electric field can influence especially the Rashba SOC of the graphene [8]. Thus we take the lowest energy configurations for graphene on hBN, as well as hBN encapsulated graphene and perform additional calculations for (α B, β H) and (H α H, B β B) configurations, where we apply a transverse electric field across the heterostructure. The electric field is modeled by a zig-zag potential.

For every magnitude of the field we calculate the low energy band structure and fit it to the model Hamiltonian. In Fig. S15 we show the fit parameters for (α B, β H) configuration as a function of external electric field. Indeed, we can tune most of the parameters. Especially the Rashba parameter can be tuned from positive to negative values, with the transition at around 2 V/nm for (α B, β H) configuration. Most important we can tune the Rashba SOC from a finite value to zero, which will heavily influence the spin relaxation. Another feature we notice is that around 2 V/nm, the PIA SOC parameters are not changing very smoothly with applied field, which is connected with the transition of the Rashba SOC through zero.

In the case of hBN encapsulated graphene we have considered (H α H, B β B) configuration and the results are shown in the main text.

SPIN RELAXATION ANISOTROPY

Since the low energy Hamiltonian \mathcal{H} can nicely reproduce the dispersion around the K point, we can use it together with our fit parameters to calculate spin relaxation times. We calculate, for a very dense k -grid in the vicinity of the K point, the energy spectrum and spin

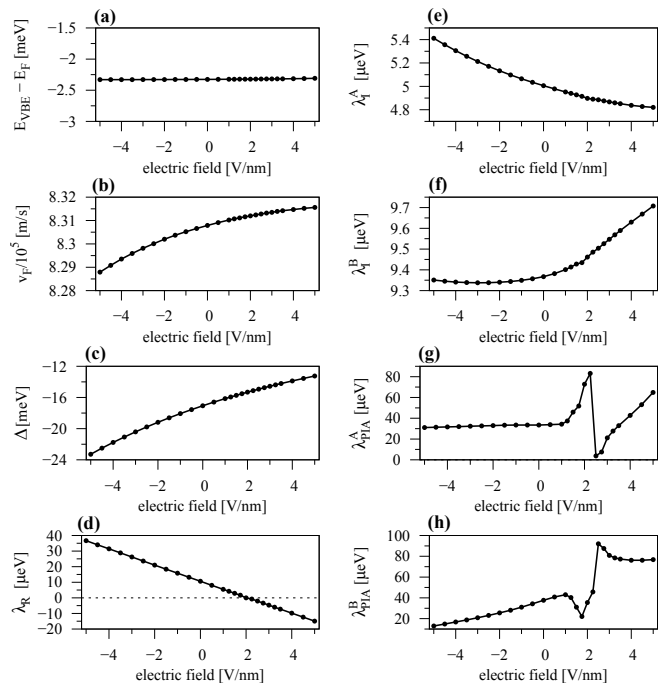


FIG. S15. (Color online) Fit parameters as a function of the applied transverse electric field for the (α B, β H) configuration. (a) Valence band edge with respect to the Fermi level, (b) the Fermi velocity v_F (c) gap parameter Δ , (d) Rashba SOC parameter λ_R , (e) intrinsic SOC parameter λ_I^A for sublattice A, (f) intrinsic SOC parameter λ_I^B for sublattice B, (g) PIA SOC parameter λ_{PIA}^A for sublattice A, and (h) PIA SOC parameter λ_{PIA}^B for sublattice B.

expectation values for the Dirac bands from our model. To calculate the spin relaxation time, we define the spin-orbit field components $\omega_{k,i}$ as

$$\omega_{k,i} = \frac{\Delta E_k}{\hbar} \cdot \frac{s_{k,i}}{s_k} \quad (S1)$$

where k is the momentum, $i = \{x,y,z\}$, and $s_{k,i}$ are the spin expectation values along a certain direction, ΔE_k is the energy splitting of the Dirac bands and $s_k = \sqrt{s_{k,x}^2 + s_{k,y}^2 + s_{k,z}^2}$ is the absolute value of the spin. By that we obtain at each k point the spin-orbit vector field. Following the derivation of Refs. 14 and 15, we then calculate the spin relaxation times as follows

$$\tau_{s,x}^{-1}(E) = \tau_p \cdot \langle \omega_{k,y}^2 \rangle + \tau_{iv} \cdot \langle \omega_{k,z}^2 \rangle \quad (S2)$$

$$\tau_{s,y}^{-1}(E) = \tau_p \cdot \langle \omega_{k,x}^2 \rangle + \tau_{iv} \cdot \langle \omega_{k,z}^2 \rangle \quad (S3)$$

$$\tau_{s,z}^{-1}(E) = \tau_p \cdot \langle \omega_{k,x}^2 + \omega_{k,y}^2 \rangle. \quad (S4)$$

The average $\langle \cdot \rangle$ is taken over all k -points that have the same constant Energy E ; τ_p is the momentum relaxation time, and τ_{iv} is the intervalley scattering time. For the calculation of the averages $\langle \cdot \rangle$ we used energy steps of 100 μ eV with a smearing of ± 50 μ eV, corresponding to a temperature of 0.58 K. Measurements [16–19] pro-

vide spin relaxation lengths of $\lambda_s \approx 20 \mu\text{m}$, spin relaxation times of $\tau_s \approx 8 \text{ ns}$, and spin diffusion constants of $D_s \approx 0.04 \frac{\text{m}^2}{\text{s}}$. With the relation $\lambda_s = \sqrt{\tau_s D_s}$ and using that the spin diffusion constant is roughly equal to the charge diffusion constant $D_s \approx D_c = \frac{1}{2} v_F^2 \tau_p$ and $v_F \approx 8 \times 10^5 \frac{\text{m}}{\text{s}}$, we get $\tau_p = 125 \text{ fs}$, which we use in the calculations. The value for τ_p is reasonable, assuming ultraclean samples. Since intervalley scattering times are hard to estimate from experiments, we take $\tau_{iv} = N \cdot \tau_p$ with $N = \{1, \dots, 15\}$ for our calculations. By that we obtain the spin relaxation time as a function of the energy, for spins along x, y, and z-direction for each ratio $N = \tau_{iv}/\tau_p$. More interesting than the individual spin relaxation times is the spin relaxation anisotropy $\xi = \tau_{s,z}/\tau_{s,x}$.

We show a colormap of the calculated anisotropy ξ as a function of N and the energy for the (αB , βH) configuration in Fig. S16(a). Within the band gap of $\pm 17 \text{ meV}$,

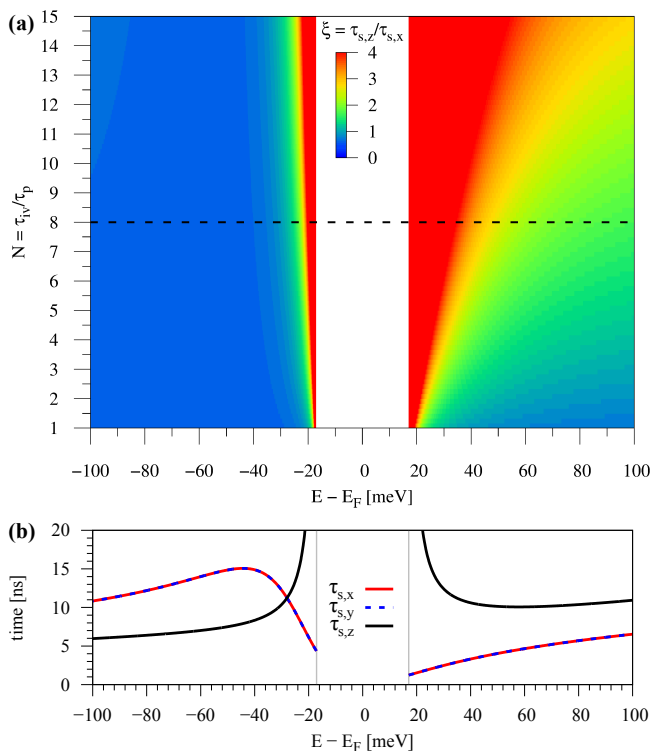


FIG. S16. (Color online) Calculated spin-relaxation times and anisotropies for (αB , βH) configuration. (a) Colormap of the spin relaxation anisotropy $\xi = \tau_{s,z}/\tau_{s,x}$ as a function of $N = \tau_{iv}/\tau_p$ and the energy. (b) Individual spin relaxation times as function of energy corresponding to the dashed line in (a) with $\tau_p = 125 \text{ fs}$ and $\tau_{iv} = 8 \cdot \tau_p$. The grey lines indicate the band edges.

of course no states are available and spin relaxation times cannot be calculated, because the smearing we use is only 0.58 K . For holes we find that the anisotropy is $\xi \approx \frac{1}{2}$ as soon as we are below -20 meV from the valence band edge, for each ratio N . For electrons the situation is com-

pletely different and the anisotropy can get very large, even 20 meV away from conduction band edge. We also find that independent of N , the anisotropy is largest close to the band edges, which would correspond to the charge neutrality point in experiment. In Fig. S16(b) we show the individual spin relaxation times as a function of energy, corresponding to $N = 8$. We find spin relaxation times up to 20 ns . However, we have to keep in mind that Fig. S16 is only valid for a certain stacking configuration of graphene on hBN.

In experiment one expects, that electrons traveling through graphene, would rather experience local spin-orbit fields that can be very different for certain regions due to the different stacking configurations. Therefore, in Fig. S17(a) we show a colormap of the calculated anisotropy ξ as a function of N and the energy when using the averaged parameters of graphene on hBN given in the main text. This averaged situation should in gen-

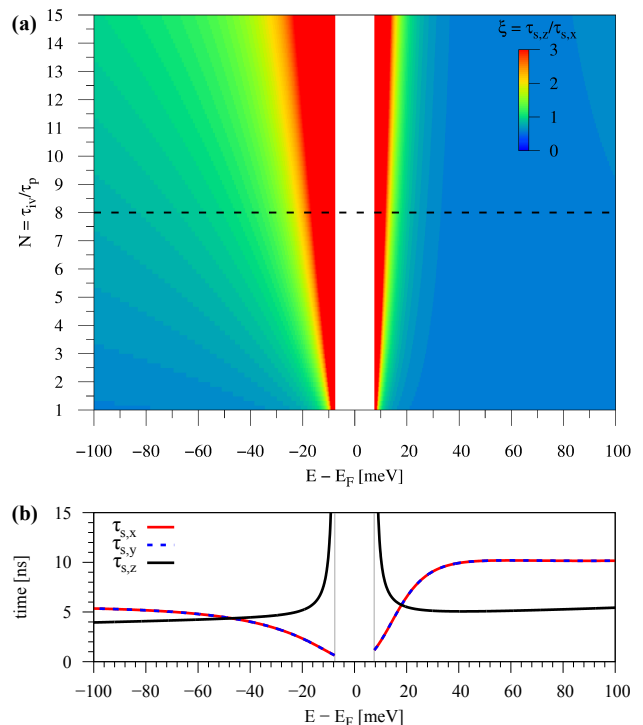


FIG. S17. (Color online) Calculated spin relaxation times and anisotropies for graphene on hBN. Here we use the averaged parameters of the graphene/hBN heterostructures given in the main text. (a) Colormap of the spin relaxation anisotropy $\xi = \tau_{s,z}/\tau_{s,x}$ as a function of $N = \tau_{iv}/\tau_p$ and the energy. (b) Individual spin relaxation times as function of energy corresponding to the dashed line in (a) with $\tau_p = 125 \text{ fs}$ and $\tau_{iv} = 8 \cdot \tau_p$. The grey lines indicate the band edges.

eral correspond to a more realistic situation in a heterostructure, where all kinds of stacking configurations are present simultaneously. We find that electrons have an anisotropy ratio $\xi \approx \frac{1}{2}$ almost independent of N and the energy, see Fig. S17(b), clearly different from the

pure (α B, β H) configuration, compare to Fig. S16. Close to the band edges, i.e. the charge neutrality point, the anisotropy can reach very large values. For holes the anisotropy varies around $\xi \approx 1$ for moderate doping densities.

So far anisotropies of $\xi \approx 1$ have been measured for graphene on hBN and SiO₂ [18, 20–23]. A first indication of large anisotropies was found in Refs. [24, 25] where it was shown that the anisotropy ξ is pronounced at the charge neutrality point and decreases with increasing carrier density. Unfortunately in this study bilayer graphene is considered and the results cannot be directly compared with our calculations here, thus only partially confirming our findings.

In Fig. S18 we show the spin relaxation anisotropy ξ , specifically for (α B, β H) configuration as function of energy and applied transverse electric field, using the parameter sets for several finite electric field strengths, see Fig. S15. We find that the anisotropy is strongly tun-

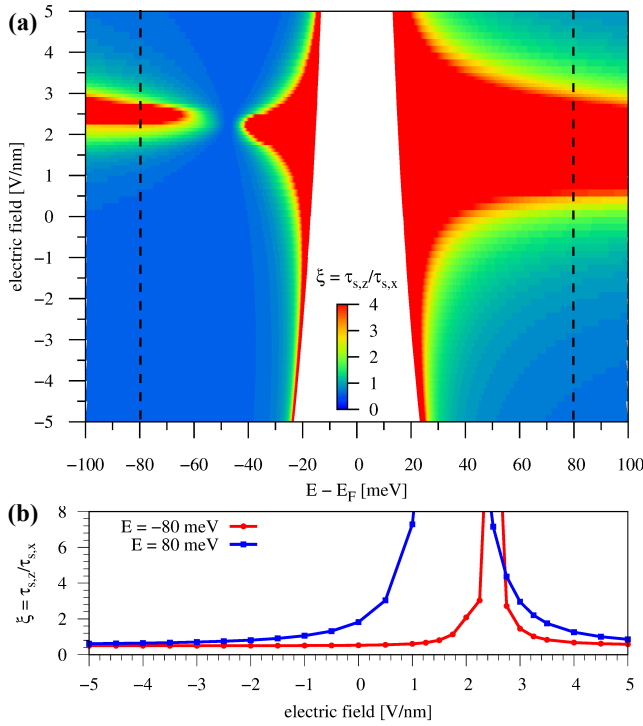


FIG. S18. (Color online) (a) Calculated spin relaxation anisotropy $\xi = \tau_{s,z}/\tau_{s,x}$ as function of energy and applied transverse electric field for (α B, β H) configuration, using $\tau_p = 125$ fs and $\tau_{iv} = 8 \cdot \tau_p$. (b) Anisotropy ξ at energies $E = \pm 80$ meV corresponding to the dashed lines in (a).

able by means of external gating. At around 2 V/nm we find a very strong enhancement of the anisotropy, which is related to the zero transition of the Rashba SOC parameter. Similar to hBN encapsulated graphene, the anisotropy is strongly increased for $\lambda_R \approx 0$, as the states are mainly s_z -polarized. By applying top and bottom gates, one can individually tune the doping level and the

electric field across the heterostructure. In Fig. S18(b) we show that an electric field can tune the anisotropy by one order of magnitude at a fixed doping level.

* klaus.zollner@physik.uni-regensburg.de

- [1] P. Blaha, K. Schwarz, G. K. H. Madsen, D. Kvasnicka, and J. Luitz, *WIEN2K, An Augmented Plane Wave + Local Orbitals Program for Calculating Crystal Properties* (Prof. Dr. Karlheinz Schwarz, Vienna University of Technology, Institute of Materials Chemistry, 2001), ISBN 3-9501031-1-2.
- [2] J. P. Perdew, K. Burke, and M. Ernzerhof, *Phys. Rev. Lett.* **77**, 3865 (1996).
- [3] S. Grimme, J. Antony, S. Ehrlich, and H. Krieg, *The Journal of Chemical Physics* **132**, 154104 (2010).
- [4] A. H. Castro Neto, F. Guinea, N. M. R. Peres, K. S. Novoselov, and A. K. Geim, *Rev. Mod. Phys.* **81**, 109 (2009).
- [5] A. Catellani, M. Posternak, A. Baldereschi, and A. J. Freeman, *Phys. Rev. B* **36**, 6105 (1987).
- [6] G. Giovannetti, P. A. Khomyakov, G. Brocks, P. J. Kelly, and J. Van Den Brink, *Physical Review B* **76**, 073103 (2007).
- [7] B. Hunt, J. D. Sanchez-Yamagishi, A. F. Young, M. Yankowitz, B. J. LeRoy, K. Watanabe, T. Taniguchi, P. Moon, M. Koshino, P. Jarillo-Herrero, et al., *Science* **340**, 1427 (2013).
- [8] M. Gmitra, S. Konschuh, C. Ertler, C. Ambrosch-Draxl, and J. Fabian, *Phys. Rev. B* **80**, 235431 (2009).
- [9] The stacking is chosen such, that each graphene sublattice has the same distance to an underlying Boron and Nitrogen atom. This seemed to be a good candidate for a gap closing, as the difference in the sublattice potential could vanish.
- [10] V. M. Pereira, A. H. Castro Neto, and N. M. R. Peres, *Phys. Rev. B* **80**, 045401 (2009).
- [11] B. Wunsch, F. Guinea, and F. Sols, *New J. Phys.* **10**, 103027 (2008).
- [12] D. Kochan, S. Irmer, and J. Fabian, *Phys. Rev. B* **95**, 165415 (2017).
- [13] R. Quhe, J. Zheng, G. Luo, Q. Liu, R. Qin, J. Zhou, D. Yu, S. Nagase, W. N. Mei, Z. Gao, et al., *NPG Asia Materials* **4**, 1 (2012).
- [14] A. W. Cummings, J. H. Garcia, J. Fabian, and S. Roche, *Phys. Rev. Lett.* **119**, 206601 (2017).
- [15] J. H. Garcia, M. Vila, A. W. Cummings, and S. Roche, *Chemical Society Reviews* **47**, 3359 (2018).
- [16] M. Drögeler, C. Franzen, F. Volmer, T. Pohlmann, L. Banszerus, M. Wolter, K. Watanabe, T. Taniguchi, C. Stampfer, and B. Beschoten, *Nano Letters* **16**, 3533 (2016).
- [17] M. Gurram, S. Omar, and B. J. van Wees, *2D Materials* **5**, 032004 (2018).
- [18] M. H. D. Guimarães, P. J. Zomer, J. Ingla-Aynés, J. C. Brant, N. Tombros, and B. J. van Wees, *Physical Review Letters* **113**, 086602 (2014).
- [19] S. Singh, J. Katoch, J. Xu, C. Tan, T. Zhu, W. Amamou, J. Hone, and R. Kawakami, *Applied Physics Letters* **109** (2016).
- [20] B. Raes, A. W. Cummings, F. Bonell, M. V. Costache,

- J. F. Sierra, S. Roche, and S. O. Valenzuela, *Physical Review B* **95**, 1 (2017).
- [21] B. Raes, J. E. Scheerder, M. V. Costache, F. Bonell, J. F. Sierra, J. Cuppens, J. Van De Vondel, and S. O. Valenzuela, *Nature Communications* **7**, 1 (2016).
- [22] S. Ringer, S. Hartl, M. Rosenauer, T. Völkl, M. Kadur, F. Hopperdietzel, D. Weiss, and J. Eroms, *Phys. Rev. B* **97**, 205439 (2018).
- [23] N. Tombros, S. Tanabe, A. Veligura, C. Jozsa, M. Popinciuc, H. T. Jonkman, and B. J. van Wees, *Phys. Rev. Lett.* **101**, 046601 (2008).
- [24] J. C. Leutenantsmeyer, J. Ingle-Aynés, J. Fabian, and B. J. van Wees, *Phys. Rev. Lett.* **121**, 127702 (2018).
- [25] J. Xu, T. Zhu, Y. K. Luo, Y.-M. Lu, and R. K. Kawakami, *Phys. Rev. Lett.* **121**, 127703 (2018).